MDPI

Article

Analysis of Efficiency Characteristics of a Deep-Sea Hydraulic Power Source

Donglin Li [1,*] **, Fuhang Guo** [1] **, Liping Xu** [1] **, Shuai Wang** [1] **, Youpeng Yan** [1] **, Xianshuai Ma** [1] **and Yinshui Liu** [2]

[1] School of Mechatronics Engineering, Henan University of Science and Technology, Luoyang 471003, China; guo212728@163.com (F.G.); xlpzz@163.com (L.X.); wang5451140@163.com (S.W.); yan99042023@163.com (Y.Y.); 18437911063@163.com (X.M.)
[2] School of Mechanical Science and Engineering, Huazhong University of Science and Technology, Wuhan 430074, China; liuwater@hust.edu.cn
[*] Correspondence: lidonglin@haust.edu.cn

Abstract: Deep-sea submersibles carry limited energy sources, so a high efficiency of the equipment is required to improve endurance. In the deep-sea environment, the hydraulic power source is filled with oil, which causes structural deformation of the power source and changes in the physical properties of the medium, leading to unknown changes in the efficiency characteristics of the power source. In order to explore the efficiency characteristics of the deep-sea hydraulic power source composed of a gear pump and a DC (direct current) brushless motor in a variable sea depth environment, we undertook the following. First, considering the effects of seawater pressure and temperature on the physical properties of the medium and the radial clearance deformation of the gear pump, a mathematical model for the total efficiency of the hydraulic power source was established. The results indicate that the deformation of the pump body is mainly determined by the seawater pressure and working pressure. Subsequently, by analyzing the effects of the two factors on the efficiency of the power source, respectively, when the oil temperature range is large enough, the total efficiency of the power source will increase and then decrease under six sea depths; the total efficiency of the power source decreases with the increase in the rotational speed. However, in a land environment, the trend of the efficiency characteristics of the power source is opposite to that of the remaining six deep-sea environments, both in terms of oil temperature and rotational speed. Finally, the efficiency trend of the power source with changes in sea depth under rated conditions was obtained. Under different sea depth ranges, the optimal operating oil temperatures and suitable rotational speed ranges of the power source could be obtained. This paper could provide a certain theoretical basis for the research and development of deep-sea equipment.

Keywords: deep-sea; hydraulic power source; structural deformation; medium physical properties; efficiency characteristic

---

1. Introduction

The ocean contains abundant biological and mineral resources, and the deep sea is the core area of the ocean, which possesses various strategic resources that are related to the future development of all humanity [1–3]. However, the exploration and development of the deep sea cannot be separated from various deep-sea equipment such as remote operated vehicles and autonomous underwater vehicles [4–6] and manned submersibles (such as Jiaolong [7,8]). Deep-sea equipment is highly dependent on deep-sea sources that provide power.

Deep-sea hydraulic power sources are widely used in the power systems of deep-sea equipment due to their excellent performance advantages such as small size, light weight, and ease in achieving stepless speed changes. Deep-sea hydraulic power sources are a closed integrated structure composed of three parts: deep-sea motor, deep-sea pump, and pressure compensator. The deep-sea motor and deep-sea pump, as well as various

blocks and sensors, are encapsulated in an oil tank, and the oil tank can avoid the direct exposure of internal devices to seawater, prevent pollutants from entering and cool mineral oil [9]. The pressure compensator can balance seawater pressure and internal pressure, avoiding the direct compression of the system structure by external pressure [10], as shown in Figure 1, showing the power source composed of a DC (direct current) brushless motor and a gear pump. The common problem with deep-sea hydraulic power sources is the relatively low total efficiency, which is due to the special environment of the deep sea: high pressure and low temperature can have a significant impact on the efficiency characteristics of the pump and motor [11,12]. In addition, seawater salinity, biological pollution, and ocean current disturbances may also have an impact on the operation of power sources, but these factors are not the most significant. The pressure of seawater mainly causes the deformation of key components of the pump and motor, which in turn affects the precise fitting clearance of the pump and motor, thereby exacerbating the friction and wear of key mating pairs. In addition, both high pressure and low temperature can cause changes in the physical properties of the oil, especially in viscosity, density and elastic modulus. The change in oil viscosity can directly affect the oil churning loss of the pump clearance and sliding bearings, the air gap and the rolling bearings of the motor [13,14].
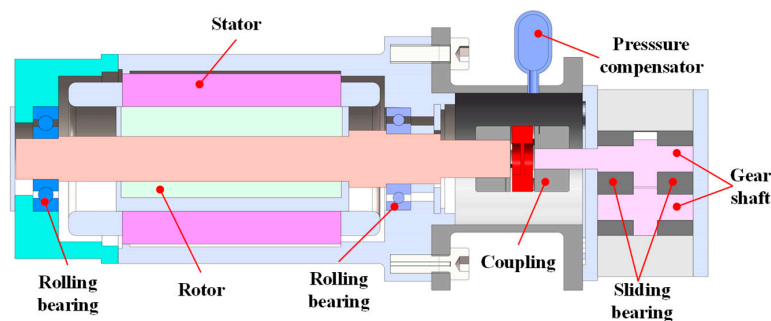

Figure 1. Schematic diagram of a hydraulic power source structure.

Tian et al. [15] investigated the efficiency characteristics of deep-sea hydraulic power sources in the full range of sea depth, and calculated the oil friction loss of the motor, the internal leakage of the gear pump and the viscous friction loss of the hydraulic system according to the power transmission process. Finally, a pressurization experiment was conducted on the prototype using a pressure cylinder, and the prototype efficiency characteristic curve was obtained as the water depth and pressure varied. Liu et al. [16] derived a seawater hydraulic axial piston motor (SHAPM) flow field pressure and torque model, and ANSYS was used to simulate the deep-sea environment, analyzing the deformation of the clearance between the piston guide rail and the sliding bearings, and finally obtaining the water depth range for the normal operation of SHAPM. Based on the linear varying parameters (LVP) theory, Cao et al. [17] proposed a novel theoretical approach model to foresee the dynamic performances of the driving unit of the deep-sea hydraulic system. In the bounded closed set of variable parameters, the dynamic characteristics of pressure and flow were obtained. The experimental results validated the rationality of the LVP method. This provides a method for predicting the working performance of a deep-sea pump.

Li et al. [18] investigated the solid–liquid two-phase fluid in a deep-sea lifting electric pump by using the DEM-CFD method. The pressure distribution and particle distribution data of the pump at different rotational speeds were obtained, and the numerical simulation was experimentally verified. Wang et al. [19] reviewed the recent advances and experimental methods of a deep-sea mining mud pump and discussed the effects of different operating parameters on the performance of the pump. This provided theoretical and experimental guidance for the development of a deep-sea mining slurry pump. Kang et al. [20] established a CFD model of a two-stage centrifugal pump by using the full flow field method and investigated the effect of the balancing hole position and size on the balancing of the axial thrust of a deep-sea mining pump. Li et al. [21] analyzed the internal

flow field of the two-stage deep-sea lifting pump at different rotational speeds and the particle flow and solid–liquid two-phase flow and other motion laws, which verified the numerical simulation with experiments.

Liu et al. [22] modeled the air gap flow field of a deep-sea oil-filled motor and analyzed the effects of air gap thickness, motor speed, oil viscosity and rotor eccentricity on the viscous drag loss, which provided a simulation method for the study of the deep-sea motor. Zou et al. [23] calculated the viscous drag loss in the air gap of a brushless DC motor with different sea depth pressures and the magnetic loss of the silicon steel sheet core by using the CFD method and finite element method, respectively. Furthermore, they experimentally verified the validity of the calculated results. Cai et al. [24] considered the characteristics of oil viscosity with sea depth pressure and temperature. Based on the viscous drag model of the brushless DC motor, a mathematical model has been established to estimate the viscous torque and experimentally confirm the inefficiency characteristics of the motor at 2 °C.

Most of the above scholars' studies considered the effect of medium property changes on viscous friction losses of a deep-sea pump and motor. However, the effect of pump pressure deformation on the efficiency characteristics has seldom been considered, and there is a lack of analysis on the total efficiency characteristics of deep-sea hydraulic power sources. For a deep-sea pump with precision fit clearance, such as a gear pump, the effects of the deformation of the pump body structure must be considered. The deep-sea motor and deep-sea pump are the core components of the deep-sea hydraulic system, and their performance directly affects the efficiency characteristics of the deep-sea hydraulic power source. Therefore, this paper comprehensively considered the changes in oil physical properties and pressure deformation and established the efficiency characteristics of a hydraulic power source composed of a DC brushless motor and gear pump. This model could to some extent replace pressure cylinder experiments simulating deep-sea environments, thereby saving manpower and material resources. Moreover, it could also provide a certain theoretical basis for the research and development of deep-sea equipment.

2. Rheology and Deformation in a Deep-Sea Environment

Considering the low-temperature characteristic of the deep-sea environment, the medium should have good low-temperature fluidity, so Kunlun YH-10 was chosen as the medium. For the KunLun YH-10, the high pressure and low temperature environment of the deep sea will have an important impact on the physical properties of the medium, mainly in the viscosity, density and bulk modulus of elasticity. Furthermore, because the radial clearance is directly related to the churning loss of rotating machinery such as a gear pump, it is also necessary to consider the high-pressure environment of the deep sea on the gear pump radial clearance deformation regarding the specific impact.

It is known that the Mariana Trench is the deepest part of the ocean, reaching up to 11,000 m [11], and sea depths ranging from 1000 m to 3000 m are easily achievable by manned submersibles, while unmanned submersibles from various countries mostly survey the deep sea between 4500 m and 7000 m [3]. Therefore, we selected six representative deep-sea environments, namely 1000 m, 2000 m, 3000 m, 4500 m, 7000 m and 11,000 m, to analyze the impact on the power source efficiency.

In this section, for comparing and analyzing the efficiency of the power source on the land environment, the physical properties of the medium and the deformation of the pump body structure were modeled and analyzed in a land environment and in six different deep-sea environments, as mentioned above.

2.1. Physical Properties of the Medium

2.1.1. Viscosity

The viscosity of KunLun YH-10 at eleven temperature points from −50 °C to 100 °C is known [25,26], and an approximate viscosity temperature curve function can be fitted as

$$\mu_{\text{te}} = p_1 T^6 + p_2 T^5 + p_3 T^4 + p_4 T^3 + p_5 T^2 + p_6 T + p_7 \tag{1}$$

where μ_{te} is the oil dynamic viscosity (Pa $\cdot$ s) at temperature T ($°$C).

The coefficients are

$$\begin{cases} p_1 = 4.421 \times 10^{-13}; p_2 = -1.648 \times 10^{-10}; p_3 = 2.501 \times 10^{-8} \\ p_4 = -1.998 \times 10^{-6}; p_5 = 9.087 \times 10^{-5}; p_6 = -0.002437 \\ p_7 = 0.04119 \end{cases} \tag{2}$$

Considering the comprehensive effects of hydraulic oil viscosity and pressure in deep-sea environments, a calculation formula can be given [27]:

$$\mu_{\text{tp}} = \mu_{\text{te}} e^{a p_{\text{s}}} \tag{3}$$

where p_s is ambient pressure (MPa), μ_{tp} is dynamic viscosity (Pa $\cdot$ s) at pressure p_{s} (MPa) and temperature T ($°$C), e is natural logarithmic base and a is pressure viscosity coefficient ($a = 0.016$ MPa^{-1}).

In a land environment, for KunLun YH-10, the surface temperature is T = 40 $°$C, $p_{\text{s}} = 0$ MPa, $\mu_{\text{tp}} = 0.0082$ Pa $\cdot$ s.

According to reference [18], when the sea depth is greater than 1000 m, the ocean current velocity can be ignored, and temperatures and pressures in six deep-sea environments can be obtained. At a depth of 1000 m, the seawater temperature is approximately 3.72 $°$C, and thereafter, as the sea depth increases, the temperature approaches 0 $°$C. At a depth of 1000 m, the seawater pressure is approximately 10 MPa, and so on for other depths. According to Equations (1)–(3), the dynamic viscosity of KunLun YH-10 corresponding to six deep-sea environments can be obtained.

2.1.2. Density

Considering the high pressure in the deep-sea environment, the compressibility of hydraulic oil cannot be ignored, and it can have an impact on density. In addition, the density of oil is also affected by environmental temperature and gas content. After a depth of 1000 m, the gas content of oil is extremely low, and oil can be considered as a pure liquid [28]. For the above six deep-sea environments, hydraulic oil can be considered as a pure liquid, and its density equation is [29] as follows:

$$\rho_{\text{tp}} = -10^{-5} p_{\text{s}}^2 + (0.0002T + 0.048)p_{\text{s}} + \rho_0 - b(T - 15°\text{C}) \tag{4}$$

where ρ_{tp} is oil density at ambient pressure p_{s} (MPa) and temperature T ($°$C), ρ_0 is the density of the oil at an atmospheric pressure and an environment of 15 $°$C, and b is oil thermal expansion coefficient (1/$°$C).

For KunLun YH-10, it is advisable to consider ρ_0 = 823.25 kg/m^3; b = 0.001/$°$C.

2.1.3. Bulk Modulus of Elasticity

From the definition of oil density, it can be concluded that

$$\begin{cases} \rho_{\text{tp}} = \rho_0/(1 - \Delta V) \\ \Delta V = p_{\text{s}}/E_{\text{tp}} \end{cases} \tag{5}$$

where ΔV is the compression volume of the oil and E_{tp} is the bulk modulus of elasticity at ambient pressure p_{s} (MPa) and temperature T ($°$C).

According to Equation (5), the bulk elastic modulus of the oil is

$$E_{\text{tp}} = p_{\text{s}}/(1 - \rho_0/\rho_{\text{tp}}) \tag{6}$$

2.2. Structural Deformation of Pump Body

Taking the working pressure of a gear pump as 28 MPa and the deep sea of 11,000 m as an example, the structural deformation of the pump body was analyzed. At this point, the external pressure on the gear pump casing was about 110 MPa. As the deformation in

the middle position of the pump body's inner wall directly affects the height of the radial clearance, the middle position of the pump body's inner wall was selected in the X and Y directions for solving. The results are shown in Figure 2.
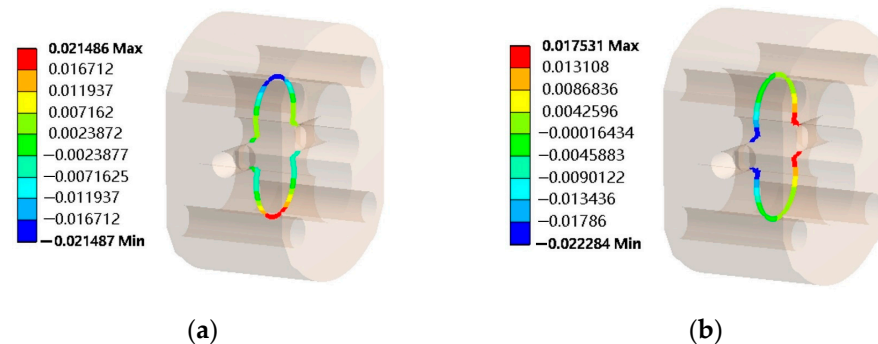

(**a**)   (**b**)

Figure 2. Deformation at the middle position of the inner wall of the pump body. (**a**) Deformation in X direction (mm); (**b**) deformation in Y direction (mm).

After the simulation was completed, we could open the output grid node settings in ANSYS to export the grid node coordinates before and after the deformation of the middle position of the pump body inner wall and draw the contour. Figure 3a shows a comparison diagram of the deformation of the middle position of the pump body inner wall after magnification 50 times. The blue scattered points represent the pump body inner wall before deformation, and the red scattered points represent the pump body inner wall after deformation.
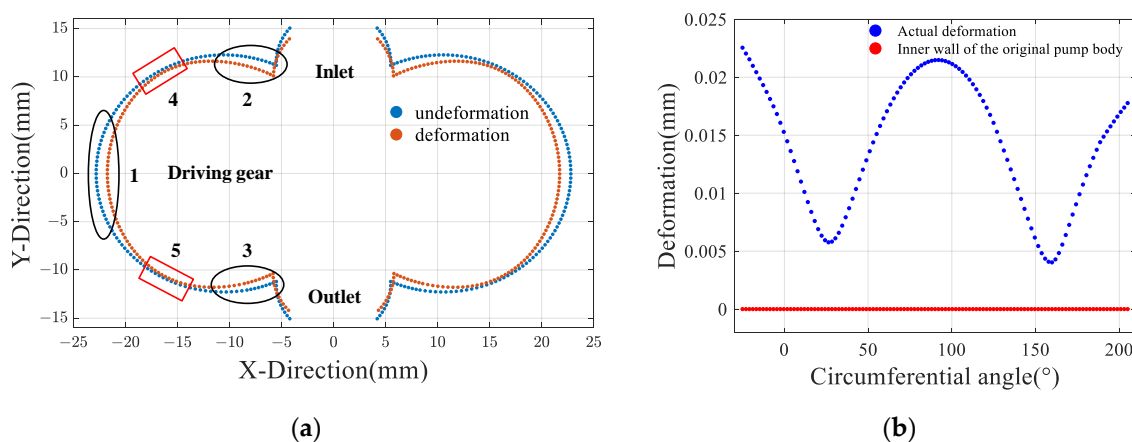

(**a**)   (**b**)

Figure 3. Deformation and circumferential expansion of the inner wall pump body in 11,000 m. (**a**) Pump body inner wall deformation; (**b**) deformation circumferential expansion.

As shown in Figure 3a, the main deformation of the inner wall of the pump body was concentrated in zone 1, zone 2 and zone 3, while the minimum deformation was concentrated in zone 4 and zone 5. It can be clearly seen that the deformation of zone 3 was smaller than that of zone 2, because zone 3 was close to the outlet, and the pressure difference was the difference between the seawater pressure and working pressure, while almost all of the pressure difference at zone 2 came from seawater pressure, which led to the overall deformation of zone 3 being smaller than that of zone 2. Because the deformation of the driving gear and driven gear was almost the same, the radial clearance deformation of the pump body inner wall corresponding to the driving gear unfolded circumferentially from the inlet to the outlet, and Figure 3b could be obtained.

The structural deformation of the inner wall of the pump body was similar to that of 11,000 m at depths ranging from 3000 m to 7000 m; because the overall seawater pressure

is greater than the working pressure at depths ranging from 3000 m to 7000 m, the inner wall of the pump body is generally in an inward compression trend. However, on land and in deep-sea environments of 1000 m and 2000 m, the seawater pressure is lower than the working pressure, which causes the inner wall of the pump body near the outlet to expand outward to a certain extent. It can be seen that the deformation of the inner wall of the pump body is jointly determined by the pressure of seawater (external pressure) and working pressure (internal pressure).

3. Establishment of the Total Efficiency Model for the Gear Pump

The research object of this paper is an external meshing gear pump with traditional involute teeth, and its power loss mainly includes the viscous friction loss of radial clearance, axial clearance, sliding bearings, and leakage power loss. Based on the CFD model of the gear pump and the structural deformation of the pump body, we established a volumetric efficiency model and a mechanical efficiency model for the gear pump, respectively. Based on the above models, a total efficiency model of the gear pump was established.

3.1. Volumetric Efficiency Model of a Deep-Sea Gear Pump

In this paper, the internal flow field of a gear pump was simulated in a surface environment as well as in six different deep-sea environments, respectively, taking into account the variations in the physical properties of the medium.

Set the boundary conditions for the inlet and outlet of the gear pump to 0.1 MPa at the inlet and 28 MPa at the outlet, and default to wall for the other boundary settings. The internal flow field simulation calculation model of the gear pump adopts the standard turbulence model and the full cavitation model. Add a symmetrical 0.01 mm axial gap on both sides to the internal flow field, and set the number of grid layers to 3. Set the gear pump speed to 5000 rpm, select KunLun YH-10 as the fluid medium, and calculate its density and dynamic viscosity based on the mathematical model in Section 2.1.

The volumetric efficiency (η_v) of the gear pump is

$$\eta_v = q / q_t \tag{7}$$

where q is actual output flow and q_t is theoretical output flow.

After the simulation has been completed, the transient outlet flow and volumetric efficiency of the gear pump can be obtained as shown in Figure 4.
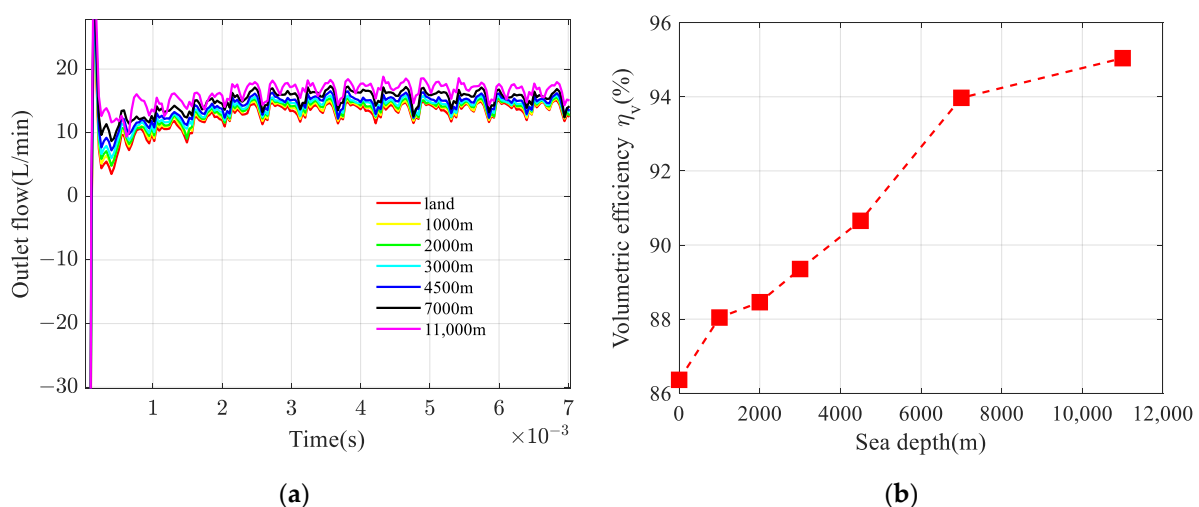

(**a**)   (**b**)

Figure 4. Transient outlet flow rate and volumetric efficiency of the gear pump. (**a**) Transient outlet flow rate; (**b**) volumetric efficiency.

As can be seen from Figure 4a, the fluctuation of the outlet flow curves of the gear pump under land and six sea depths are similar. And the outlet flow and volumetric efficiency of the gear pump gradually increases with the increase in sea depth, as shown in Figure 4b. This is because as the sea depth increases, the viscosity of the oil will also increase, which reduces the internal leakage of the gear pump and increases the volumetric efficiency.

3.2. Mechanical Efficiency Model of a Deep-Sea Gear Pump
3.2.1. Viscous Friction Loss in Radial Clearance

Considering that the inner wall of the pump body will deform in a deep-sea environment, we introduced a deformation $d_{\mathrm{r}} = d_{\mathrm{r}}(\theta)$ (see Figure 3); at this time, the circumferential distribution corresponding to the radial clearance of the driving gear was no longer uniform. The corrected radial clearance height ($h(\theta)$) is

$$h(\theta) = \delta - d_{\mathrm{r}} \tag{8}$$

where θ is the wrap angle of the corresponding radial clearance area and δ is the uniform radial clearance height.

In this polar coordinate system, take counterclockwise as positive, and the circumferential wrap angle corresponding to the radial clearance area of the driving gear is shown in Figure 5. The center O is the center of the driving gear, and the direction of the vector $\overrightarrow{Ox}$ is the polar axis. The angle between the starting edge of the radial gap area and the polar axis is -25°, and the angle between the ending edge and the polar axis is 205°. Converted to radians, that is

$$-\frac{5\pi}{36} \le \theta \le \frac{41\pi}{36} \tag{9}$$

or the leakage of the radial clearance i, the leakage of the radial clearance of the gear pump is simplified as a gap flow between parallel plates, with the pressures of the adjacent two tooth spaces being p_i and p_{i-1}, respectively, and the direction of the pressure difference being opposite to the direction of movement of the tooth tip. From the gap flow theory, it can be found that velocity (u) is [30]:

$$\begin{cases} u = \frac{y(h_i - y)}{2\mu S}\Delta p_i - (1 - \frac{y}{h_i})u_0 \\ u_0 = \frac{2\pi n}{60}r_a \end{cases} \tag{10}$$

where h_i is the height of radial clearance i, Δp_i is the pressure difference between adjacent tooth spaces of the radial clearance i ($\Delta p_i = p_i - p_{i-1}$, in units of Pa), u_0 is the tooth tip rotation speed (m/s), n is the gear shaft speed (r/min), r_a is the gear tip circle radius (m) and μ is the oil dynamic viscosity (Pa · s).
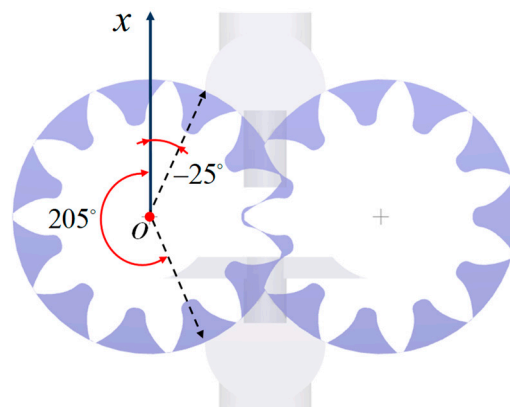

Figure 5. Polar coordinate schematic diagram of radial clearance flow field of the driving gear.

In order to obtain the circumferential pressure distribution of the gear pump during stable operation, monitoring points can be added to the circumferential contour of the central section of the internal flow field of the gear pump, as shown in Figure 6a. Starting from point1 of the radial clearance of the driving gear and ending at the point47, a total of 47 monitoring points were added every 5°. The monitoring point type was set to stationary.
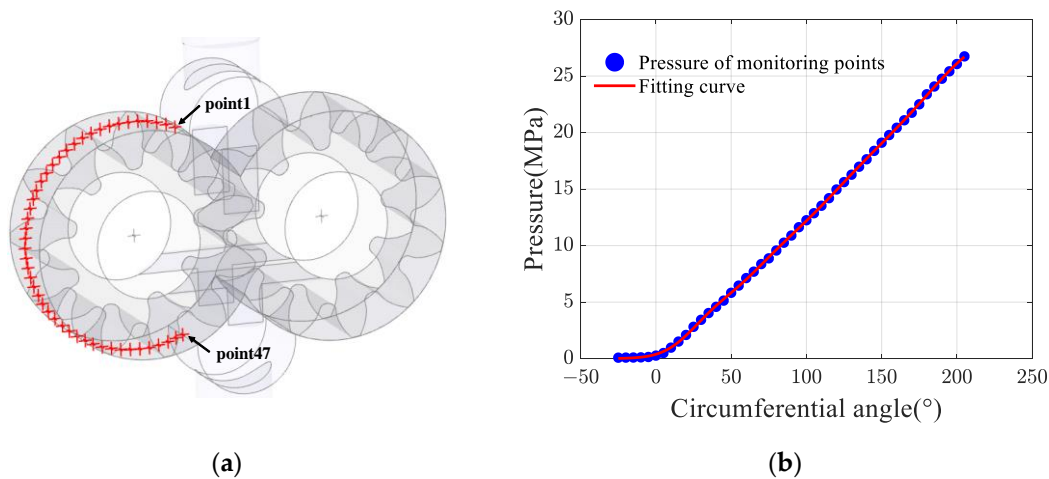

(**a**)   (**b**)

Figure 6. Pressure distribution of radial clearance of driving gear: (**a**) 47 monitoring points; (**b**) circumferential pressure distribution.

After the convergence of the simulation calculation was completed, the average pressure values for each of the 47 monitoring points were calculated, and then the fitting toolbox provided with MATLAB (R2010, Henan University of Science and Technology, Luoyang, China) was used to perform curve fitting to obtain the circumferential pressure fitting distribution curve of the driving gear. As shown in Figure 6b, this is the circumferential pressure distribution of the gear pump on land.

The fitting function is

$$p_r(\theta) = a_1 \mathrm{e}^{-\left(\frac{\theta-b_1}{c_1}\right)^2} + a_2 \mathrm{e}^{-\left(\frac{\theta-b_2}{c_2}\right)^2} + a_3 \mathrm{e}^{-\left(\frac{\theta-b_3}{c_3}\right)^2} + a_4 \mathrm{e}^{-\left(\frac{\theta-b_4}{c_4}\right)^2} \tag{11}$$

The coefficients are

$$\begin{cases} a_1 = 8.674 \times 10^6; b_1 = 123.7; c_1 = 56.95 \\ a_2 = 2.765 \times 10^7; b_2 = 229.3; c_2 = 86.8 \\ a_3 = 3.582 \times 10^6; b_3 = 69.96; c_3 = 37.59 \\ a_4 = 1.594 \times 10^6; b_4 = 35.7; c_4 = 23.92 \end{cases} \tag{12}$$

For the radial clearance i, the pressure difference Δp_i and Δp_{i-1} of adjacent tooth spaces can be given by Equations (11) and (12).

According to Equations (10) and (11), the viscous friction power loss (W_{pr}) between all tooth tip end faces of a single gear and the inner wall of the pump body can be obtained as

$$W_{\mathrm{pr}} = \sum_{i=1}^{Z_{\mathrm{p}}} BS \cdot \tau\big|_{y=0} \cdot u_0 = Bu_0 \sum_{i=1}^{Z_{\mathrm{p}}} \left(\frac{h_i}{2} \cdot \Delta p_i + \frac{u_0}{h_i} S\mu\right) \tag{13}$$

where $\tau\big|_{y=0} = \mu[(\mathrm{d}u/\mathrm{d}y)\big|_{y=0}]$ is shear stress (Pa) at the tooth tip end face, Z_{p} is teeth number corresponding to radial clearance for a single gear, B is gear width (m) and S is tooth tip thickness (m).

3.2.2. Viscous Friction Loss of Axial Clearance

The total viscous friction loss (W_{ps}) in the axial clearance of the gear pump is [31] as follows:

$$W_{ps} = \frac{1}{25}\pi^3 n^2 \frac{\mu}{\delta_a}[\frac{1}{18}(r_b{}^4 - r_s{}^4) + \frac{1}{27}r(r_a{}^3 - r_b{}^3)]$$ (14)

where δ_a is axial clearance height (m), r_b is root circle radius (m), r_s is gear shaft radius (m) and r is pitch radius (m).

3.2.3. Viscous Friction Loss of Sliding Bearings

The viscous friction loss (W_{pb}) of a single sliding bearing is

$$W_{pb} = C_f \mu D_{bs}{}^2 B_{bs} \omega^2$$ (15)

where C_f is frictional coefficient, D_{bs} is bearing inner diameter, B_{bs} is axial thickness of bearing and ω is gear shaft angular velocity ($\omega = 2\pi n/60$, in units of rad/s).

For the external meshing gear pump, there are two radial clearances and four sliding bearings, so the total viscous friction loss (W_{pf}) of the gear pump is recorded as

$$W_{pf} = 2W_{pr} + W_{ps} + 4W_{pb}$$ (16)

The theoretical output power (P_t) of the gear pump is

$$P_t = p \cdot q_t$$ (17)

where p is actual working pressure (Pa) and q_t is theoretical output flow rate (m^3/s).

Therefore, the mechanical efficiency (η_m) of the gear pump is

$$\eta_m = \frac{T_t \omega}{T \omega} = \frac{T_t \omega}{T_t \omega + W_{pf}}$$ (18)

where T_t is theoretical torque of the gear pump ($T_t = 9550\frac{P_t}{n}$, in units of N · m) and T is the actual torque of the gear pump (N · m).

3.3. Total Efficiency Model of the Deep-Sea Gear Pump

The total leakage power loss (W_{pl}) of the gear pump is

$$W_{pl} = (1 - \eta_v)P_t$$ (19)

Based on the above analysis, the total efficiency (η_p) of the gear pump can be obtained as

$$\eta_p = \eta_v \cdot \eta_m$$ (20)

4. Total Efficiency Model of the Hydraulic Power Source

The viscous friction power loss of an electric motor mainly consists of two parts. One part is the viscous friction loss in the air gap between the rotor and stator. As the speed increases, the flow field in the air gap is almost turbulent, with a small part being the transitional flow. There is an energy exchange between fluid particles, so the empirical formula is not applicable for calculating viscous friction loss here [22]. For the calculation of air gap viscous friction loss, this section is provided by fluid simulation. The other part is the viscous friction loss of rolling bearings, which is given by the formula.

4.1. Viscous Friction Loss of the Air Gap of the Deep-Sea Motor

The structural parameters of the DC brushless motor mainly include motor speed n = 5000 r/min, outer radius of rotor r_m = 101.75 mm and internal radius of stator r_s = 100 mm. The bearings of the motor use 6006 deep-groove ball bearings, and the

flow resistance coefficient of the ball can be determined using the Reynolds number, according to Table 1.

Table 1. Flow resistance coefficient [23].

Reynolds number Re	10^{-1}	1	10	10^2	10^3	10^4	10^5
Flow resistance coefficient	275	30	4.20	1.20	0.48	0.40	0.40

Similarly, under land and six deep-sea environments, the software Fluent was used to simulate the oil-immersed working environment of the motor, and a two-dimensional simulation model of the air gap was established as shown in Figure 7. The rotation of the inner wall of the rotor was driven by a UDF (user defined functions) dynamic grid, and the outer wall of the stator was set as stationary. Set the simulation step number to 10,000 steps with a step size of 1×10^{-6}.
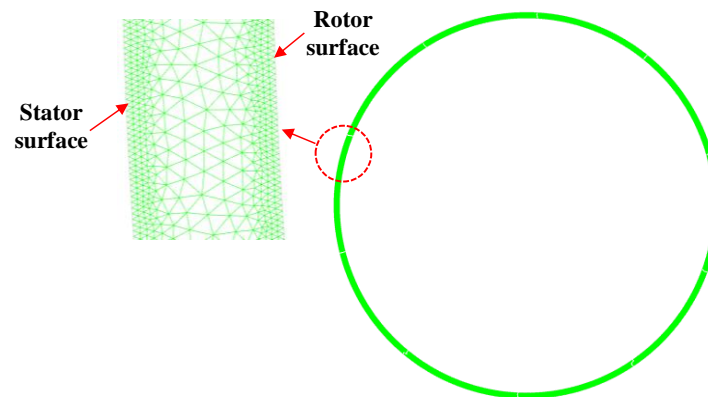

Figure 7. Air gap simulation model.

After the convergence of the calculation was completed, the torque in the rotor area could be calculated using the forces under the report option in Fluent. The simulation results can be obtained as follows.

As shown in the partially enlarged image of Figure 8, the torque fluctuation stabilized towards 0.01 s. The viscous friction torque value of the air gap was negative, indicating that the direction of the torque was counterclockwise.
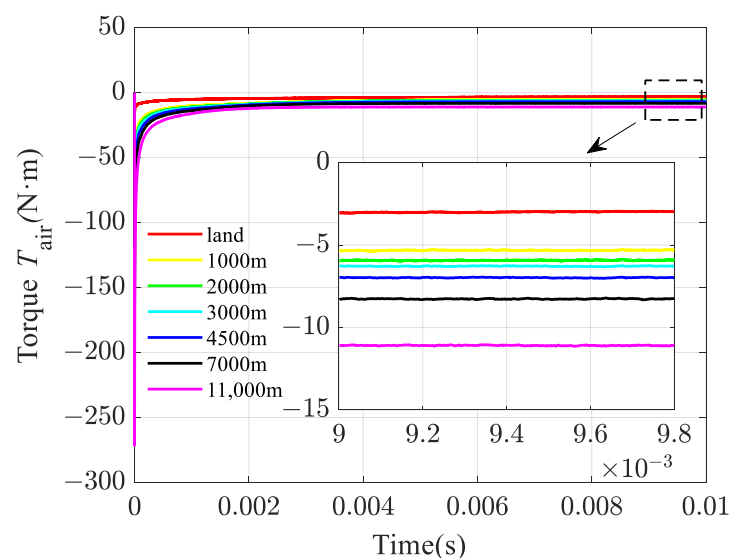

Figure 8. Air gap torque under different environments.

The viscous friction torque of the motor air gap is (T_{air}), so the viscous friction loss (W_{air}) of the air gap is

$$W_{\text{air}} = T_{\text{air}}\omega \tag{21}$$

4.2. Viscous Friction Loss of Deep-Sea Motor Bearings

When the rolling element of a rolling bearing rotates in a bearing filled with oil, it is subjected to the flow resistance and the rolling element itself is subjected to the stirring friction torque of the fluid. For deep-groove ball bearings, the flow resistance (F_d) of each ball is [32] as follows:

$$F_d = \frac{\pi}{32}C_{\text{d}}\rho(D_{\text{w}}d_{\text{m}}\omega_{\text{m}})^2 \tag{22}$$

where C_{d} is flow resistance coefficient, ρ is oil density (kg/m^3), D_{w} is ball diameter (m), d_{m} is bearing pitch diameter (m) and ω_{m} is the angular velocity of the bearing cage (rad/s).

The Reynolds number (Re) is

$$Re = \frac{\rho V D_{\text{w}}}{\mu} \tag{23}$$

where V is ball center revolution linear speed (m/s) and μ is oil dynamic viscosity.

The ball center revolution linear speed (V) is

$$V = \frac{1}{2}d_{\text{m}}\omega_{\text{m}} \tag{24}$$

The diameter of the bearing pitch circle (d_{m}) is

$$d_m \approx \frac{1}{2}(d + D) \tag{25}$$

where d is bearing inner diameter (m) and D is bearing outer diameter (m).

The theoretical angular velocity of bearing cage (ω_{m}) is [32] as follows:

$$\omega_{\text{m}} = \frac{\omega_e(1 + \gamma) + \omega_i(1 - \gamma)}{2} \tag{26}$$

where ω_e is the angular velocity of the bearing outer ring ($\omega_e = 0$, in units of rad/s), ω_i is the angular velocity of the bearing inner ring ($\omega_i = \omega$, in units of rad/s) and γ is the dimensionless number of bearings.

The dimensionless number of bearings γ is [32] as follows:

$$\gamma = \frac{D_{\text{w}}\cos\alpha_{\text{b}}}{d_{\text{m}}} \tag{27}$$

where α_{b} is the bearing contact angle (for deep groove ball bearings, $\alpha_{\text{b}} = 0$).

The viscous friction loss of a single ball is denoted as (W_{mb}), so it can be obtained as

$$W_{\text{mb}} = F_d \cdot V \tag{28}$$

Because the motor has two bearings, the viscous friction loss (W_{mrb}) of all the balls in the motor is

$$W_{\text{mrb}} = 2N_{\text{ball}}W_{\text{mb}} \tag{29}$$

where N_{ball} is the number of balls per bearing.

Therefore, the total viscous friction loss (W_{mf}) of the motor is

$$W_{\text{mf}} = W_{\text{mrb}} + W_{\text{air}} \tag{30}$$

Therefore, the total efficiency (η_e) of the motor is

$$\eta_e = \frac{P_m - W_{mf}}{P_m} \tag{31}$$

where P_m is the motor output power (P_m = 13 kW).

4.3. Total Efficiency Model of the Power Source

From the above analysis, it can be concluded that the total efficiency (η_h) of the hydraulic power source is

$$\eta_h = \eta_p \cdot \eta_e \tag{32}$$

5. Factors Affecting the Efficiency of the Hydraulic Power Source

This section mainly analyzes the impact of oil temperature, rotational speed and rated condition on the efficiency characteristics of the hydraulic power source, respectively. The main structural parameters of the gear pump are shown in Table 2.

Table 2. The main structural parameters of the gear pump.

Properties	Symbol	Driving Gear	Driven Gear
Modulus (mm)	m	1.81	1.81
Number of teeth	Z	11	11
Pressure angle	α	20°	20°
Gear shaft radius (mm)	r_s	5.75	5.75
Gear width (mm)	B	10.6	10.6
Tooth tip thickness (mm)	S	0.96	0.96
Radial clearance (mm)	δ	0.04	0.04

5.1. The Influence of Oil Temperature on Power Source

When the hydraulic power source is in deep-sea operation, the electric motor and gear pump are fully both immersed in the oil. As the motor drives the gear pump to rotate, the friction loss between the two and the oil will be converted into heat, causing the temperature of the oil to rise. The temperature rise of the oil will lead to changes in viscosity, which in turn will affect the viscous friction loss of the motor and gear pump. Therefore, it is necessary to study the impact of changes in oil temperature on the efficiency characteristics of the power source.

5.1.1. The Influence of Oil Temperature on the Gear Pump

Relevant references indicate that the temperature rise of oil in deep-sea environments can reach 40 °C [33], so the temperature range of oil is determined to be between 0 °C and 40 °C. For this hydraulic power source, an interval of 10 °C can be observed within this temperature range, with a total of five temperature points taken for research. When the speed of the gear pump is 5000 rpm and the working pressure is 28 MPa, the power loss distribution map of the gear pump at corresponding temperature points in different environments can be obtained.

As shown in Figure 9a, the impact of different oil temperatures on the total viscous friction loss of the gear pump is similar in various environments. Taking land as an example, it can be seen that the viscous friction loss decreases with the increase in oil temperature. This is because the viscosity of the oil decreases with the increase in temperature, thus reducing the viscous friction loss. By comparing the effects of different environments at the same temperature on the viscous friction loss of gear pump, taking 0 °C as an example, it can be seen that the viscous friction loss increases with the increase in sea depth. This is because the oil viscosity increases with the increase in sea depth, thereby increasing the viscous friction loss. And, interestingly, as the sea depth increases, the difference in viscous friction loss between the five temperatures in each environment also increases,

which fully demonstrates that oil temperature has a significant impact on viscous friction loss in deep-sea environments.
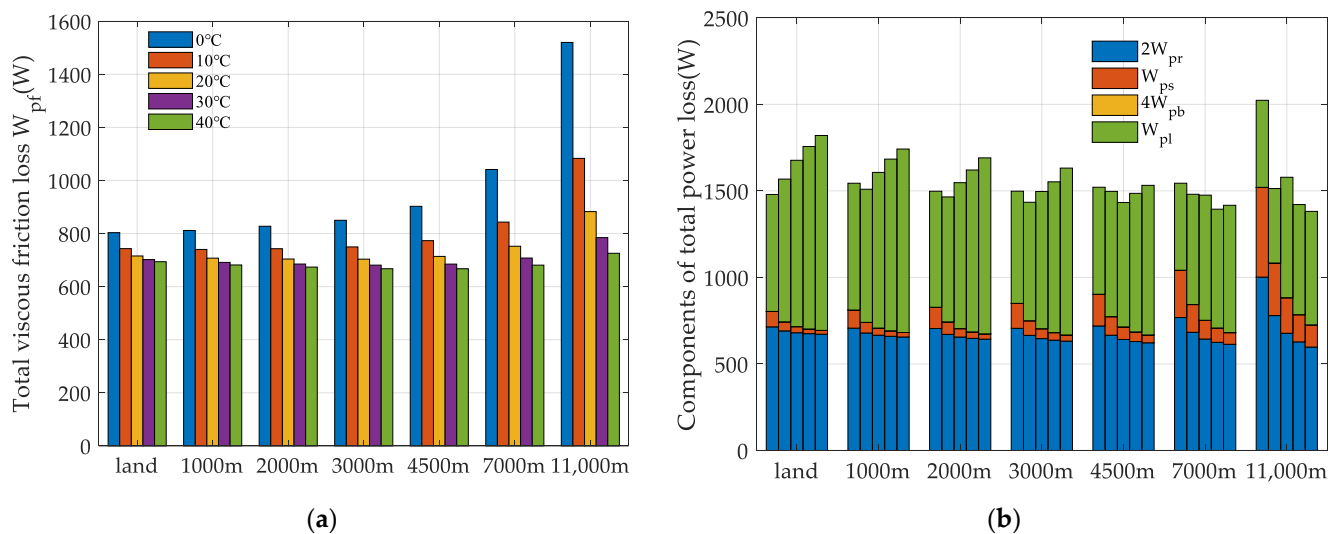

Figure 9. Power loss of the gear pump at different temperatures. (**a**) Total viscous friction loss of the gear pump; (**b**) total power loss components of the gear pump.

Figure 9b shows the power loss components of the gear pump, which are partially composed of the total viscous friction loss of radial clearance, axial clearance and the sliding bearings; the other part is total leakage power loss. In the deep-sea range of land of ~3000 m, the main reason is that leakage power loss accounts for a large proportion. This is because at low sea depths, the relative change in oil viscosity is not significant, resulting in a slight decrease in leakage power loss. At the same time, viscous friction loss does not increase sharply. However, at depths of 4500 m~11,000 m, as the viscosity of the oil increases sharply, it suppresses the internal leakage of the gear pump and also exacerbates the power loss due to viscous friction, which accounts for a large proportion of viscous friction loss.

5.1.2. The Influence of Oil Temperature on the Motor

Similarly, at a motor speed of 5000 rpm, the air gap is simulated using Fluent and the following results can be obtained.

As shown in Figure 10a, for the deep-sea motor, the trend of total viscous friction loss is similar to that of the gear pump. The reason is the same and will not be repeated. Figure 10b shows the power loss component of the motor, consisting of the viscous friction power loss of the air gap and rolling bearings. It can be seen that the viscous friction loss in the air gap accounts for the majority of the total power loss of the motor, while the viscous friction loss in rolling bearings accounts for a small proportion compared to the air gap.

From Figure 11, it can be seen that the total efficiency of the power source in a land environment always decreased with the increase in temperature. This is because in this environment, the oil viscosity itself is very low, and as the temperature increases, it will become lower. This will exacerbate the leakage power loss of the gear pump, thereby reducing efficiency. For power sources at depths ranging from 1000 m to 4500 m in the deep sea, the total efficiency first increases and then decreases with increasing temperature. This is because the rapid decrease in viscous friction loss due to temperature rise leads to an increase in efficiency. However, when the temperature exceeds a certain threshold, it will cause the viscosity of the oil to be too low, which increases the leakage power loss and leads to a decrease in efficiency. For power sources at depths of 7000 m and 11,000 m, the total efficiency of the power source continuously increases with increasing temperature. This is because within this temperature range, the influence of pressure on oil viscosity is

greater than that of temperature, which leads to an increase in the total efficiency of the power source. It can be foreseen that as the oil temperature continues to rise, starting from 40 °C, the total efficiency of the power source at depths of 7000 m and 11,000 m will begin to decrease after a certain temperature point.
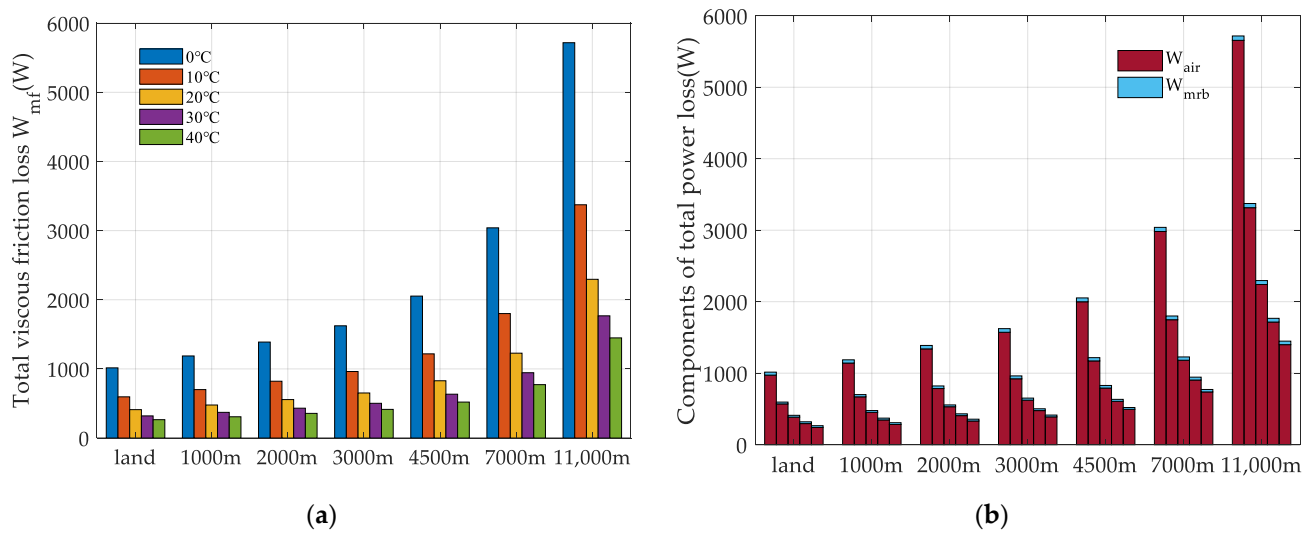

Figure 10. Power loss of the motor at different temperatures. (**a**) Total viscous friction loss of motor; (**b**) total power loss components of motor.
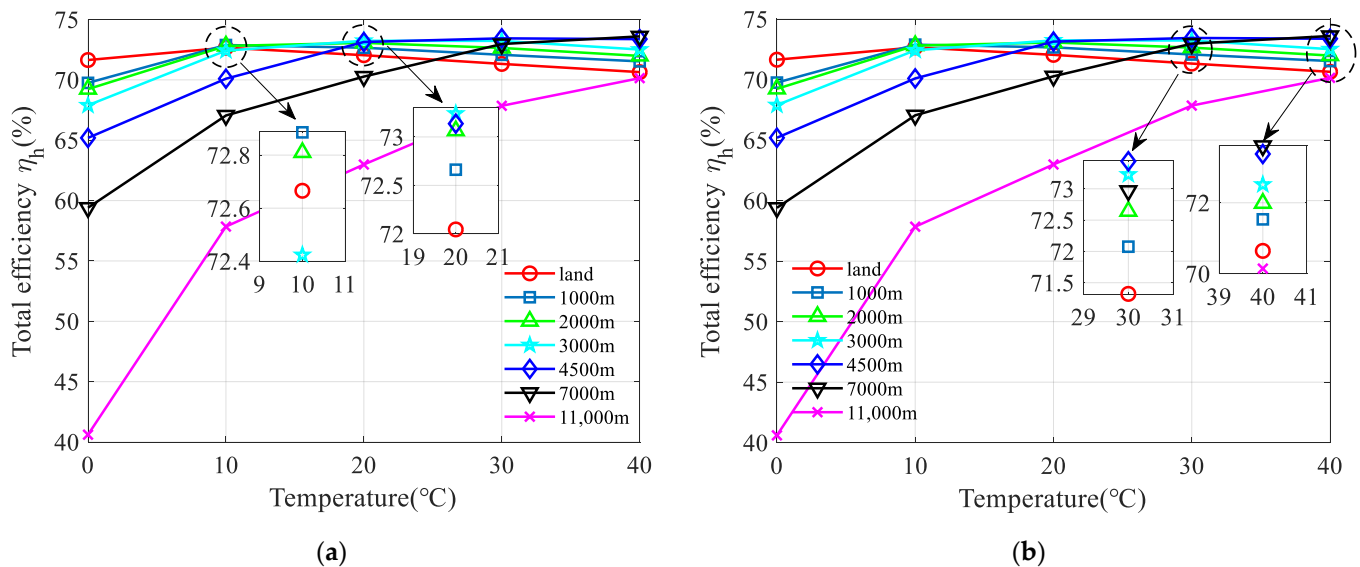

Figure 11. Total efficiency of power sources at different temperatures: (**a**) 10 °C and 20 °C; (**b**) 30 °C and 40 °C.

5.2. The Influence of Rotational Speed on the Power Source

The working pressure of the fixed gear pump was 28 MPa, and the speed range of the motor and gear pump was set to 1000 rpm~5000 rpm. For the hydraulic power source, a total of five speeds were studied by increasing by 1000 rpm each time within this speed range.

5.2.1. The Influence of Rotational Speed on the Gear Pump

Based on the above working conditions, the power loss distribution map of the gear pump corresponding to the speed in different environments can be obtained.

As shown in Figure 12a, the impact of different rotational speeds on the total viscous friction loss of the gear pump was similar in various environments. Taking land as an example, it can be seen that the viscous friction loss increased with the increase in speed, because the flow of oil is more prone to turbulence as the speed increases, thus increasing the viscous friction loss. By comparing the effects of different environments on the viscous friction loss of the gear pump at the same speed, taking 1000 rpm as an example, it can be seen that the viscous friction loss increases with the increase in sea depth. This is because the oil viscosity increases with the increase in sea depth, thereby increasing the viscous friction loss. And interestingly, as the sea depth increases, the difference in viscous friction loss under the five different rotational speeds in various environments also increases, which fully demonstrates that rotational speed has a significant impact on viscous friction loss in deep-sea environments.

Similarly, Figure 12b shows the power loss components of the gear pump. In the same environment, the leakage power loss of the gear pump will decrease with the increase in speed, because the volumetric efficiency of the gear pump increases with the increase in speed, thereby reducing internal leakage and reducing the leakage power loss. Fixed at a certain speed, taking 1000 rpm as an example, it is evident that the leakage power loss of the gear pump decreases rapidly with the increase in sea depth. This is because as the sea depth increases, the viscosity of the oil will sharply increase, which will reduce internal leakage and reduce the leakage power loss.
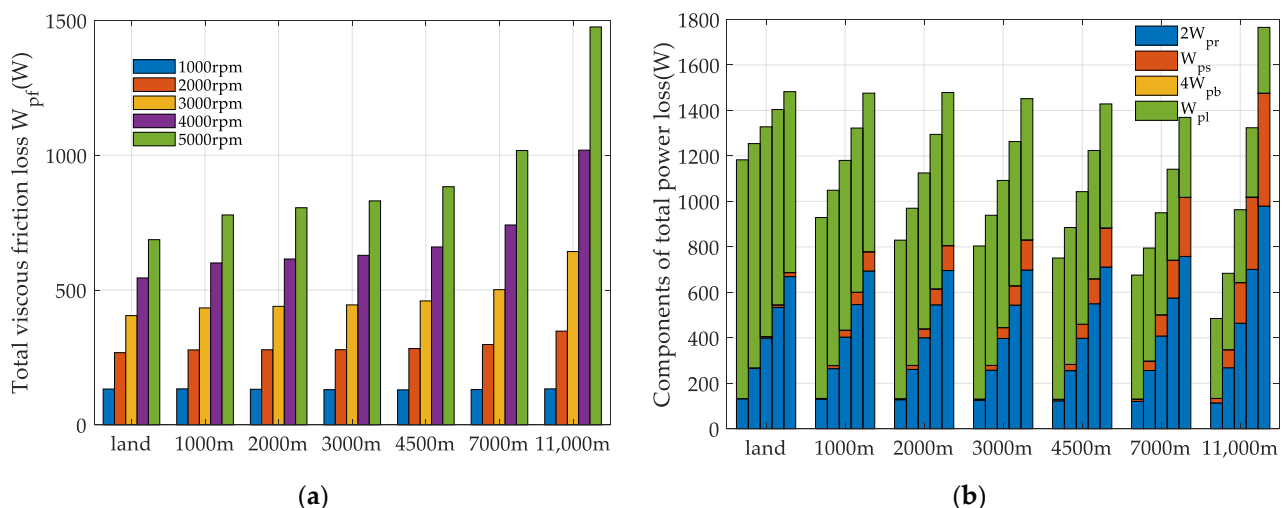

Figure 12. Power loss of the gear pump at different speeds. (**a**) Total viscous friction loss of the gear pump; (**b**) total power loss components of the gear pump.

5.2.2. The Influence of Rotational Speed on the Motor

As shown in Figure 13a, for the deep-sea motor, the trend of total viscous friction loss is similar to that of the gear pump. The reason is the same and will not be repeated. Figure 13b shows the power loss component of the motor, consisting of the viscous friction power loss of the air gap and rolling bearings. It can be seen that the viscous friction loss in the air gap accounts for the majority of the total power loss of the motor, while the viscous friction loss in rolling bearings accounts for a small proportion compared to the air gap.

As shown in Figure 14, in a land environment, the total efficiency of the power source always increases with the increase in speed. This is because in this environment, the oil viscosity is very low, and the viscous friction loss increases relatively little with the increase in speed. However, the leakage power loss of the gear pump decreases with the increase in speed, and the combination of the two increases the efficiency of the power source. In the other six deep-sea environments, the total efficiency of the power source decreases with the increase in rotational speed. This is because as the rotational speed increases, the viscous friction loss gradually increases, thereby reducing efficiency.
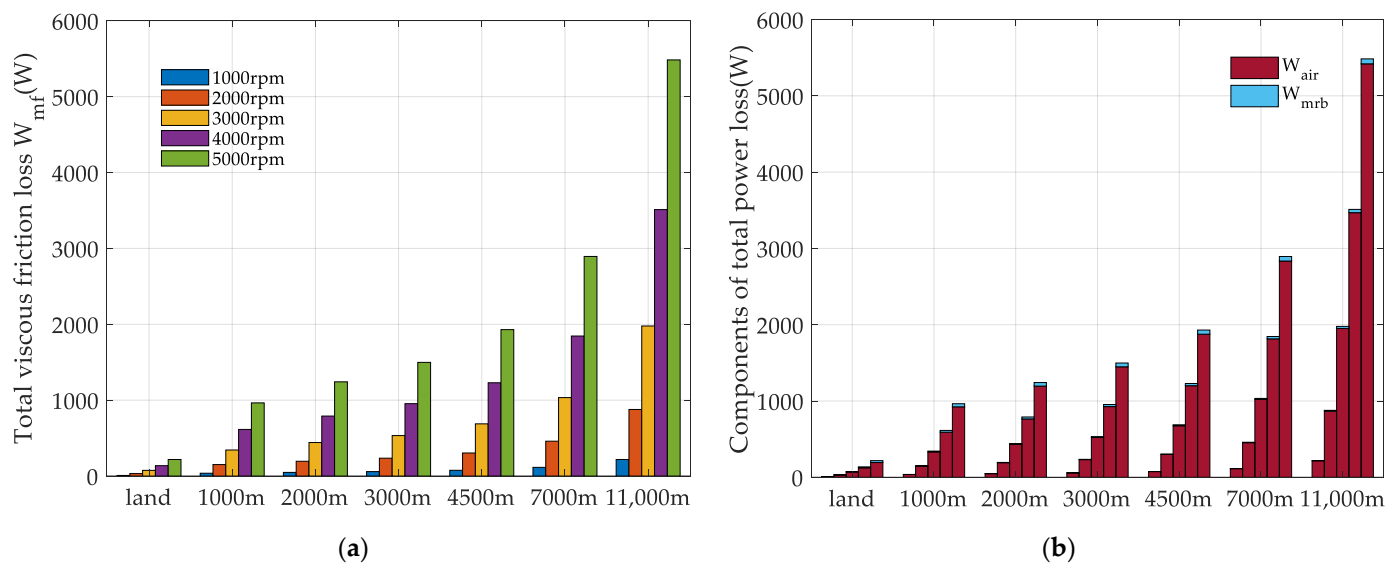
Figure 13. Power loss of the motor at different speeds. (**a**) Total viscous friction loss of the motor; (**b**) total power loss components of the motor.
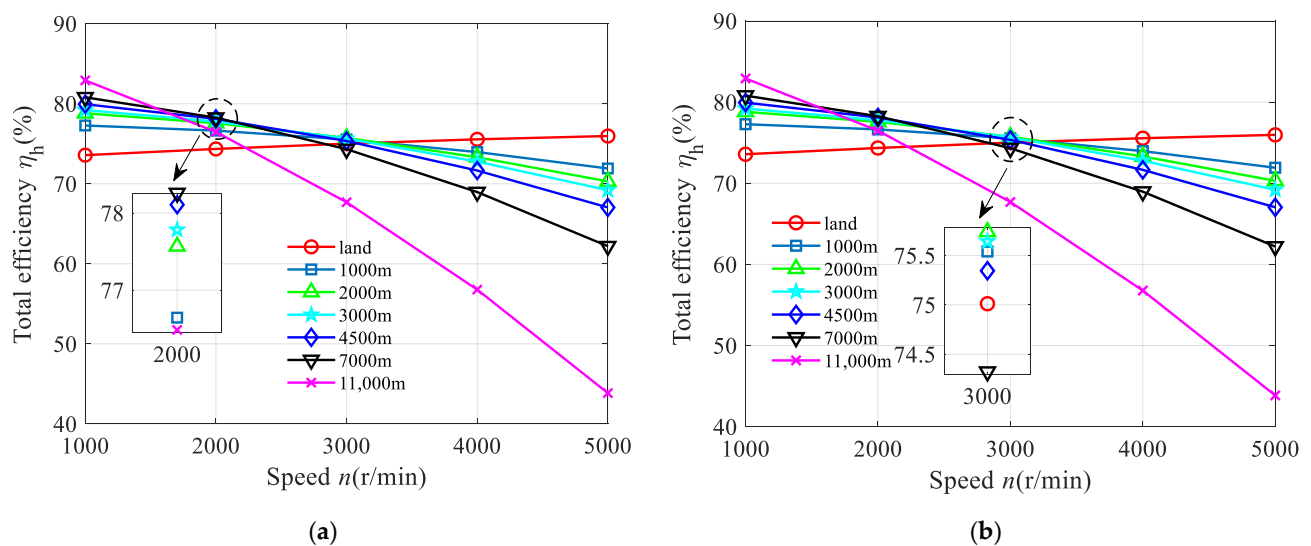

Figure 14. Total efficiency of power sources at different speeds: (**a**) 2000 rpm; (**b**) 3000 rpm.

5.3. The Influence of the Rated Condition on the Power Source

On land and in six deep-sea environments, the efficiency characteristics of the hydraulic power source under the rated operating speed of 5000 rpm and a gear pump working pressure of 28 MPa can be obtained from mathematical models.

5.3.1. The Influence of the Rated Condition on the Gear Pump

Based on the established mathematical model, the efficiency characteristics of the gear pump can be calculated, as shown in Figure 15. As shown in Figure 15a, the mechanical efficiency of the gear pump decreases with the increase in sea depth. This is because as the sea depth increases, the seawater pressure will cause a decrease in precision clearance and a sharp increase in oil viscosity, which will exacerbate the mechanical and friction losses of the gear pump. As shown in Figure 15b, the total efficiency of the gear pump first increases and then decreases with the increase in sea depth, which is consistent with the experimental trend in reference [15]. This is because the volumetric efficiency of the gear pump (see Figure 4) shows an opposite trend to the mechanical efficiency, and theoretically there exists

an optimal working depth with the highest efficiency. For the gear pump studied in this paper, its optimal working depth was around 7000 m.
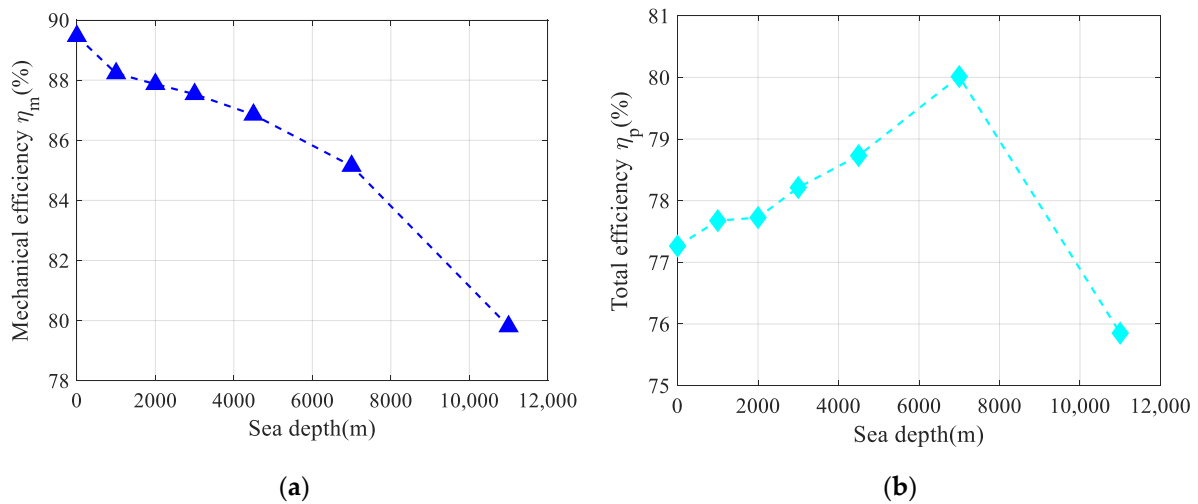

(**a**)

(**b**)

Figure 15. The efficiency characteristics of the gear pump. (**a**) Mechanical efficiency of the gear pump; (**b**) total efficiency of the gear pump.

5.3.2. The Influence of the Rated Condition on the Motor

Similarly, the total efficiency characteristics of the motor and the power source can be obtained. As shown in Figure 16a, the total efficiency of the motor decreased with increasing sea depth, which is consistent with the experimental trend in reference [15]. As shown in Figure 16b, the total efficiency of the power source decreased with increasing sea depth. Compared to the total efficiency trend of the power source in reference [15], in this paper, the total efficiency trend of the power source was different because it did not consider the power loss of the hydraulic circuit. Moreover, considering the pressure cylinder experiment in reference [15], the oil tank temperature was basically stable at around 32 °C. In fact, on land, it is difficult for the pressure cylinder to simulate the low-temperature environment of the deep sea, which can result in significant differences between the efficiency data of the gear pump and the motor calculated in this paper and the experimental data in reference [15].
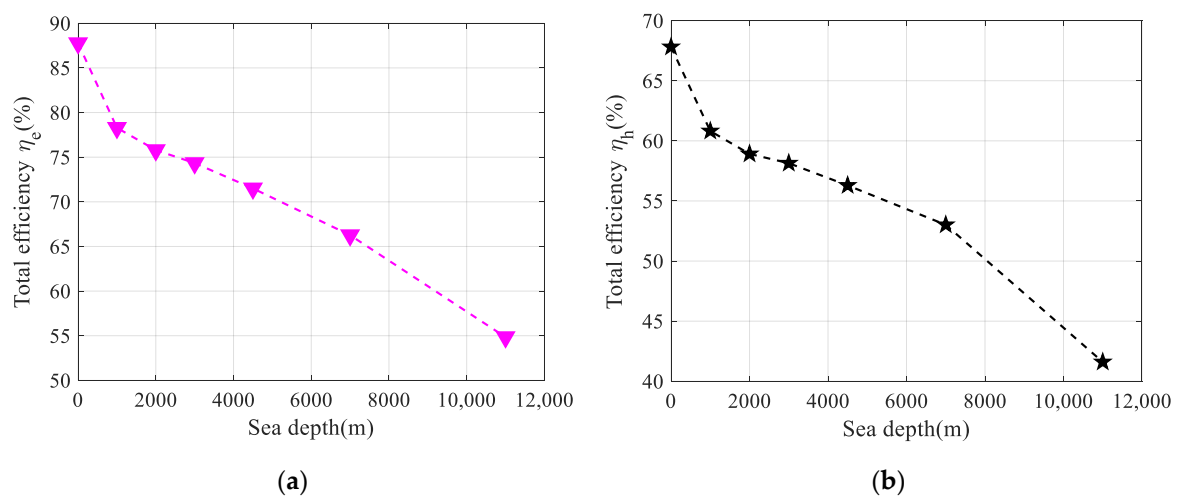

(**a**)

(**b**)

Figure 16. The total efficiency of the motor and the power source. (**a**) Total efficiency of the motor; (**b**) total efficiency of the power source.

6. Discussion

This paper comprehensively considers the effects of seawater pressure and temperature on the physical properties of the medium, innovatively introduces the influence of structural deformation of a gear pump in a deep-sea environment on radial clearance, establishes an efficiency model of a hydraulic power source and obtains relevant results. However, this paper focuses on the derivation and analysis of mathematical models, and there is currently a lack of experimental verification. Subsequent experiments should be conducted to verify the accuracy of the model. In addition, this paper should consider other environmental factors that may affect deep-sea hydraulic power sources, such as seawater salinity, solid particles, and external interference. These simplifications may result in an inability to capture the true behavior of hydraulic systems. Finally, in different deep-sea environments, selecting different mediums may different effects on the efficiency of the power source, and it is necessary to compare the effects of three or more mediums on it in the future.

7. Conclusions

In this work, the efficiency model of the power source has been established and the efficiency characteristics of the power source have been investigated in three aspects, namely oil temperature, rotational speed and rated condition, on land and in six deep-sea environments, respectively. Based on the study, the following conclusions can be obtained.

(1) By analyzing the efficiency characteristics of the power source with changes in sea depth under a rated working condition, it is known that the mechanical efficiency of the gear pump decreases with the increase in sea depth, which has the opposite trend to the volumetric efficiency. In theory, the optimal working sea depth of the gear pump is calculated to be around 7000 m. The power loss of the motor mainly comes from the viscous friction loss in the air gap, and the total efficiency of the power source has been decreasing with the increase in sea depth.

(2) By analyzing the impact of oil temperature on the efficiency characteristics of the power source, it can be concluded that in four deep-sea environments, ranging from 1000 m to 4500 m, the total efficiency of the power source first increases and then decreases with the increase in temperature. However, for the power source at depths of 7000 m and 11,000 m, their total efficiency increased with increasing temperature. This indicates that the optimal operating oil temperature of the power source varies depending on sea depth. Similarly, it can be concluded that the total efficiency of the power source decreases with increasing rotational speed in six deep-sea environments. However, in a land environment, both the oil temperature and speed, the efficiency characteristics of the power source, tended to be opposite to the other six deep-sea environments.

(3) Based on the analysis of the impact of the above two factors on the efficiency characteristics of the power source, for the power source operating at depths of 7000 m~11,000 m, the operating oil temperature is suitable for above 40 °C, and the rotational speed is suitable for 1000 rpm~2000 rpm. For the power source operating at depths of 1000 m~4500 m, the operating oil temperature is suitable at around 20 °C, and the rotational speed is suitable for 2000 rpm~3000 rpm.

Based on the above findings, the efficiency characteristics of the hydraulic power source operating in a deep-sea environment are very sensitive to changes in oil temperature, especially in sea depths exceeding 4500 m. Therefore, we could set up a separate heating source inside the hydraulic power source, or add throttle components and shorten the return oil pipeline in the hydraulic system. Through feedback from temperature sensors and by matching appropriate speed ranges, we can selectively adjust the oil temperature to improve the efficiency of the power source.

Author Contributions: Methodology and writing—original draft preparation, D.L. and F.G.; test and data processing, L.X. and S.W.; project administration, Y.Y.; checking and supervision, X.M. and Y.L. All authors have read and agreed to the published version of the manuscript.

Data Availability Statement: The data-supported results are included within this article.

Conflicts of Interest: The authors declare no conflict of interest.

References

1. Cao, X.P.; Wang, X.J.; Deng, B.; Ke, J. Development status and key technologies of deep-sea hydraulic power sources. *Ocean Bull.* **2010**, *29*, 466–471.
2. Lin, M.W.; Yang, C.J. Ocean Observation Technologies: A Review. *Chin. J. Mech. Eng.* **2020**, *33*, 18. [CrossRef]
3. Kang, Y.; Liu, S. The development history and latest progress of deep-sea polymetallic nodule mining technology. *Minerals* **2021**, *11*, 1132. [CrossRef]
4. Sahoo, A.; Dwivedy, S.K.; Robi, P.S. Advancements in the field of autonomous underwater vehicle. *Ocean Eng.* **2019**, *181*, 145–160. [CrossRef]
5. Ludvigsen, M.; Sorensen, A.J. Towards integrated autonomous underwater operations for ocean mapping and monitoring. *Annu. Rev. Control* **2016**, *42*, 145–157. [CrossRef]
6. Ahn, J.; Yasukawa, S.; Sonoda, T.; Ura, T.; Ishii, K. Enhancement of deep-sea floor images obtained by an underwater vehicle and its evaluation by crab recognition. *J. Mar. Sci. Technol.* **2017**, *22*, 758–770. [CrossRef]
7. Cui, W.C. Development of the *Jiaolong* Deep Manned Submersible. *Mar. Technol. Soc. J.* **2013**, *47*, 37–54. [CrossRef]
8. Zhang, T.W.; Tang, J.L.; Qin, S.J.; Wang, X.X. Review of Navigation and Positioning of Deep-sea Manned Submersibles. *J. Navig.* **2019**, *72*, 1021–1034. [CrossRef]
9. Tic, V.; Lovrec, D. Design of modern hydraulic tank using fluid flow simulation. *Int. J. Simul. Model.* **2012**, *11*, 77–88. [CrossRef]
10. Wu, J.B.; Li, L.; Wei, W. Research on dynamic characteristics of pressure compensator for deep-sea hydraulic system. *Proc. Inst. Mech. Eng. Part M- J. Eng. Marit. Environ.* **2022**, *236*, 19–33. [CrossRef]
11. Liu, Y.S.; Cheng, Q.; Wang, Z.Y.; Pang, H.; Deng, Y.P.; Zhou, X.P.; Luo, X.H.; Cui, Y.; Wu, D.F. Seawater hydraulics: From the sea surface to depths of 11,000 meters. *Sci. China-Technol. Sci.* **2022**, *65*, 2178–2189. [CrossRef]
12. Liu, Y.S.; Wu, D.F.; Li, D.L.; Deng, Y.P. Application and Research Progress of Deep Sea Hydraulic Technology. *J. Mech. Eng.* **2018**, *54*, 14–23. [CrossRef]
13. Chao, Q.; Tao, J.F.; Liu, C.L.; Li, Z.L. Development of an analytical model to estimate the churning losses in high-speed axial piston pumps. *Front. Mech. Eng.* **2022**, *17*, 11. [CrossRef]
14. Concli, F.; Gorla, C. Analysis of the oil squeezing power losses of a spur gear pair by mean of cfd simulations. In Proceedings of the 11th ASME Biennial Conference on Engineering Systems Design and Analysis, (ESDA 2012), Nantes, France, 2–4 July 2012; pp. 177–184.
15. Tian, Y.Q.; Liu, S.; Long, J.C.; Chen, W.; Leng, J.X. Analysis and Experimental Research on Efficiency Characteristics of a Deep-Sea Hydraulic Power Source. *J. Mar. Sci. Eng.* **2022**, *10*, 35. [CrossRef]
16. Liu, Y.S.; Deng, Y.P.; Fang, M.S.; Li, D.L.; Wu, D.F. Research on the torque characteristics of a seawater hydraulic axial piston motor in deep-sea environment. *Ocean Eng.* **2017**, *146*, 411–423. [CrossRef]
17. Cao, X.P.; Ye, M.; Deng, B.; Zhang, C.H.; Yu, Z.Y. LVP modeling and dynamic characteristics prediction of a hydraulic power unit in deep-sea. *China Ocean Eng.* **2013**, *27*, 17–32. [CrossRef]
18. Li, Y.W.; Liu, S.J.; Hu, X.Z. Research on rotating speed's influence on performance of Deep-Sea lifting motor pump based on DEM-CFD. *Mar. Geores. Geotechnol.* **2019**, *37*, 979–988. [CrossRef]
19. Wang, R.K.; Zhu, Z.C.; Su, X.H.; Mianowicz, K.; Jia, H.; Wu, K.X. Slurry pumps in deep-sea mining: A review of numerical and experimental studies. *Ocean Eng.* **2022**, *251*, 22. [CrossRef]
20. Kang, Y.J.; Su, Q.; Liu, S.J. On the axial thrust and hydraulic performance of a multistage lifting pump for deep-sea mining. *Ocean Eng.* **2022**, *265*, 11. [CrossRef]
21. Li, Y.W.; Guo, Z.M.; Liu, S.J.; Hu, X.Z. Flow Field and Particle Flow of Two-Stage Deep-Sea Lifting Pump Based on DEM-CFD. *Front. Energy Res.* **2022**, *10*, 15.
22. Liu, J.T.; Yan, L.; He, X.H.; Zhou, Y.C.; Yu, Z.H. Analysis of Oil Viscous Drag Loss of Deep-sea Motor Based on CFD Method. In Proceedings of the 17th Conference on Industrial Electronics and Applications (ICIEA), Chengdu, China, 16–19 December 2022; pp. 1289–1293.
23. Zou, J.B.; Qi, W.J.; Xu, Y.X.; Xu, F.; Li, Y.; Li, J.J. Design of Deep Sea Oil-Filled Brushless DC Motors Considering the High Pressure Effect. *IEEE Trans. Magn.* **2012**, *48*, 4220–4223. [CrossRef]
24. Cai, M.J.; Wu, S.J.; Yang, C.J. Effect of Low Temperature and High Pressure on Deep-Sea Oil-Filled Brushless DC Motors. *Mar. Technol. Soc. J.* **2016**, *50*, 83–93. [CrossRef]
25. Yao, C.J.; Chen, X.H.; Li, Y.L.; Wang, X.P. Online Viscosity Monitoring Technology for Equipment Hydraulic Oil. *Chin. Hydraul. Pneum.* **2018**, *02*, 81–85.

26. Chen, Z.D.; Ji, H.T.; Li, L.L.; Gu, L.; Hu, X.H.; Ma, Y.X.; Li, B.P. Experimental Study on Hydraulic Source of Deep Manned Submarine. *Chin. Hydraul. Pneum.* **2023**, *47*, 11–18.
27. Cao, X.P.; Zhou, Z.Q.; Wang, G.H.; Zhang, C.H.; Yang, B. Study on Change Rules of Oil Viscosity Characteristics Based on Deepening Environment Model. *Lubr. Eng.* **2017**, *42*, 1–6.
28. Cao, X.P.; Wei, C.C.; Zhao, S.G.; Cao, H.Q. Study on the Change Law of Oil Density Characteristics Based on Deep Sea Environment Model. *Lubr. Eng.* **2020**, *45*, 41–46.
29. Karjalainen, J.P.; Karjalainen, R.; Huhtala, K. An extended second order polynomial model for hydraulic fluid density. In Proceedings of the ASME/BATH 2013 Symposium on Fluid Power and Motion Control, Sarasota, FL, USA, 6–9 October 2013.
30. Mucchi, E.; Dalpiaz, G.; del Rincòn, A.F. Elastodynamic analysis of a gear pump. Part I: Pressure distribution and gear eccentricity. *Mech. Syst. Signal Proc.* **2010**, *24*, 2160–2179. [CrossRef]
31. Wei, Q.; Jing, B.D.; Bao, D.H.; Yang, L.J. Design & Study on CBZb2-based External Gear Pump Optimum Clearance. In Proceedings of the 13th International Manufacturing Conference in China, Dalian, China, 21–23 September 2009; pp. 203–208.
32. Ebert, F.J. Fundamentals of Design and Technology of Rolling Element Bearings. *Chin. J. Aeronaut.* **2010**, *23*, 123–136. [CrossRef]
33. Cai, L.F.; Zhang, J.; Fang, Y.T.; Huang, X.Y. CFD-based flow and temperature field analysis of deep-sea oil-filled motor. In Proceedings of the 24th International Conference on Electrical Machines and Systems (ICEMS), Gyeongju, Republic of Korea, 31 October–3 November 2021; pp. 1118–1121.